

1 **Semi-automatic Ice Rafted Debris quantification with Computed Tomography**

2 Jan Magne Cederstrøm<sup>1</sup>, Willem G.M. van der Bilt<sup>1</sup>, Eivind W.N. Støren<sup>1</sup> and Sunniva Rutledal<sup>1</sup>

3 <sup>1</sup>Department of Earth Science, University of Bergen, Allégaten 41, 5007 Bergen, Norway and  
4 Bjerknes Centre for Climate Research, Bergen, Norway.

5

6 \*Corresponding author: Willem G.M. van der Bilt ([willemvanderbilt@uib.no](mailto:willemvanderbilt@uib.no))

7

8 **Key Points:**

- 9 • CT counting reproduces the known number of particles added to phantom archives.
- 10 • CT counting tracks the main trends in published IRD profiles from sediment archives.
- 11 • CT counting improves the sampling resolution to resolve higher-frequency variability.

12

13

14

15

16

17

18

19

20

21

22

23 **Abstract**

24

25 Sedimentary Ice Rafted Debris (IRD) provides critical information about the climate sensitivity  
26 and dynamics of ice sheets. In recent decades, high-resolution investigations have revealed ice  
27 rafting events in response to rapid warming: such reconstructions help us constrain the near-  
28 future stability of our planet's fast-changing cryosphere. However, similar efforts require  
29 laborious and destructive analytical procedures to separate and count IRD. Computed  
30 Tomography (CT) holds great promise to overcome these impediments to progress by enabling  
31 the micrometer scale visualization of individual IRD grains. This study demonstrates the  
32 potential of this emerging approach by **1)** validating CT counts in synthetic sediment archives  
33 (phantoms) spiked with a known number of grains, **2)** replicating published IRD stratigraphies,  
34 and **3)** improving sampling resolution. Our results show that semi-automated CT counting of  
35 grains in the common 150-500  $\mu\text{m}$  size fraction reproduces actual particle numbers and tracks  
36 manually counted trends. We also find that differences between manual and CT-counted data are  
37 explained by image processing artifacts, offsets in sampling resolution and bioturbation. By  
38 acquiring these promising results using basic image processing tools, we argue that our work  
39 advances and broadens the applicability of ultra-high resolution IRD counting with CT to deepen  
40 our understanding of ice sheet-climate interactions on human-relevant timescales.

41

42

43

44

45

46 **Plain Language Summary**

47

48 Chunks of ice regularly break off glaciers floating in the ocean. These icebergs contain rock  
49 fragments picked up during the journey from land to water. As icebergs drift into warmer waters  
50 and melt, this rubble sinks to the bottom and settles on the ocean floor. Detection of these  
51 particles in marine sediments thus provide evidence that glacial ice reached down to sea-level.  
52 The flux of this ice rafted debris (IRD) gives researchers information about the past behavior of  
53 glaciers. As our planet warms, melting glaciers have become important drivers of sea-level rise.  
54 IRD studies can therefore help us better adapt to rising sea levels. But to do so on timescales  
55 relevant for humans, researchers have to extract thousands of samples from meters of sediment  
56 and sieve out IRD grains before manually counting them. Faster approaches would greatly ease  
57 the workload. In this study, we present a promising way to do so with the help from a medical  
58 technique: Computed Tomography (CT). Our findings show it is possible to semi-automatically  
59 count sand-sized grains from CT imagery without touching or destroying samples. We also show  
60 that this can be done with simple processing steps accessible to non-experts.

61

62

63

64

65

66

67

68

69

70

71 **1 Introduction**

72

73 Along glaciated margins, the calving and rafting of melting icebergs from marine-terminating  
74 glaciers deliver Ice Rafted Debris (IRD) to the open ocean (Ruddiman, 1977). The presence and  
75 concentration of IRD grains in marine sediment sequences provides critical information about ice  
76 sheet dynamics (Andrews, 2000). Over the past decades, such investigations have revealed  
77 enigmatic phases of millennial-scale ice sheet instability – notably Heinrich (H) events,  
78 Dansgaard-Oeschger (D-O) cycles and Bond events (Bond et al., 1992, Dansgaard et al., 1993,  
79 Heinrich, 1988) – which have attracted significant research activity. Greater spatial coverage and  
80 a higher sampling resolution of IRD reconstructions allow us to better understand the pattern,  
81 pace and causes of these extreme events to better assess future ice sheet stability (e.g. Hemming,  
82 2004).

83

84 Such efforts are, however, hampered by the time-consuming laboratory work that is required to  
85 separate IRD grains from background sediments, and subsequently count individual particles.  
86 Typical steps include multiple rounds of manually weighing, and sieving material into different  
87 grain size fractions. In addition, size requirements often limit the sampling resolution of records,  
88 while the counting of split samples due to time constraints may introduce uncertainty (e.g. Van  
89 der Plas & Tobi, 1965). Evidently, (semi)-automated non-destructive approaches have significant  
90 potential to advance the field by **1)** reducing analysis time, **2)** improving sampling resolution,  
91 and **3)** preserving valuable core material for other analyses. Over the past decades, researchers  
92 have proposed various approaches to do so, and key examples include the use of semi-automated  
93 particle size counting or the investigation of 2-D and 3-D X-Ray images (e.g., Andrews et al.,  
94 1997, Becker et al., 2018, , Ekblom Johansson et al., 2020, Jennings et al., 2018, Grobe, 1987).

95 However, while the semi-automated approach (e.g. Becker et al. 2018) is destructive and  
96 requires a series of manual steps, others only target the coarsest size fraction or rely on 2-D  
97 imagery (e.g. Grobe, 1987) so that counts are not reported per weight or volume as is customary  
98 in the literature.

99

100 This study explores the potential of 3-D X-Ray Computed Tomography (CT) to overcome the  
101 foresaid limitations. This approach distinguishes grains from host sediment based on density  
102 differences. Recent increases in resolution and sampling size have shown great promise to detect  
103 and count barely visible particles in sediment volumes (e.g. Fouinat et al., 2017, Hodell et al.,  
104 2017, Røthe et al., 2018). Here, we advance the ability of CT to semi-automatically detect and  
105 count IRD particles by **1)** designing an experiment based on synthetic sediment records spiked  
106 with varying, but known, number of particles of the commonly analyzed 150-500  $\mu\text{m}$  size  
107 fraction, **2)** validating our experimental findings by comparing CT and manual particle counts on  
108 published conventionally analyzed IRD records, and **3)** demonstrating that high-resolution CT  
109 counts capture high-frequency variability that is not captured by standard manual sampling  
110 protocols.

111

## 112 **2 Materials and Methods**

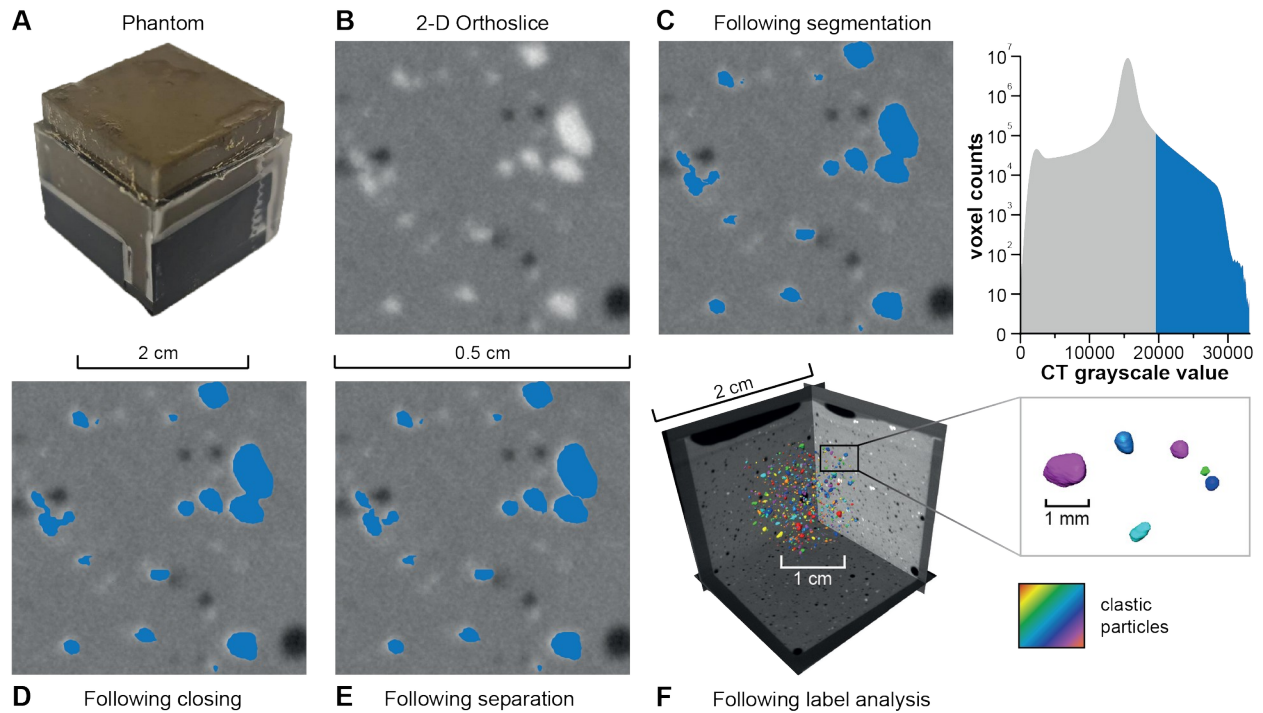
113

### 114 **2.1 Experimental design**

115

116 To explore the capability of CT to detect and count IRD particles within a sediment matrix, we  
117 designed a controlled experiment using synthetic sediment archives (phantoms). For this  
118 purpose, we filled 20 standard 8  $\text{cm}^3$  plastic cubes with a calculated number of 150-500  $\mu\text{m}$

119 grains mixed in a marine sediment matrix (Fig. 1A). To cover the typical range of IRD  
 120 concentrations identified in published reconstructions, we added circa 25, 100, 500, 1000 and  
 121 2000 grains per gram of dry weight ( $\text{g}^{-1}$  dry sediment).



122 **Figure 1.** Imagery that highlights key steps of our experimental approach. (a) close-up of one of  
 123 the created synthetic records - phantoms. (b) a raw  $0.25 \text{ cm}^2$  2-D cross-section (orthoslice) from  
 124 one of our phantoms – note how dense radiopaque (light) clastic particles stand out. (c)  
 125 thresholded particles following iterative segmentation (see section 2.4). The histogram on the  
 126 right shows the applied CT greyscale value thresholds. (d) Restoration of fuzzy object  
 127 boundaries (see section 2.4). (e) Separation of adjoining particles. (f) Individually classified  
 128 (colored) clastic particles in a  $1 \text{ cm}^3$  3-D visualization (reconstruction) used for subsequent  
 129 sieving and counting.

131

132 Counting three extracts of a known weight in triplicate, with the help of a Leica MZ6 optical  
 133 microscope under  $\times 40$  magnification, allowed us to establish a robust relation between weight

134 and particle counts whilst quantifying the human counting error. To assess the effect of  
135 lithological differences on our results, we created four sets of phantoms that were each spiked  
136 with bedrock types that are commonly found in major IRD source areas: quartz (density of 2.65  
137 g/cm<sup>3</sup>), basalt (density of 3.0 g/cm<sup>3</sup>), dolomite (density of 2.8 g/cm<sup>3</sup>), and a 1:1:1 mixture of  
138 these materials (e.g., Bond et al., 1992, Jullien et al., 2006). For this purpose, we respectively  
139 relied on commercial quartz sand, basaltic floodplain sediments from northern Iceland and a  
140 dolomite laboratory standard (see Fig. S1). The mineralogy of each material was ascertained  
141 using a Bruker D8 ADVANCE ECO X-Ray diffractometer, equipped with a 1.5418 Å Copper  
142 (Cu) source operated at 40 kV/25 mA (see Fig. S2). Sensu Hemming (2004), we identify grains  
143 larger than 150 µm as IRD-sized and consequently only added material retained on a 150 µm  
144 mesh. To remove large visible grains, we also sieved out clasts larger than 2 mm. To assess the  
145 ability of CT imagery to reproduce sample particle size distributions, we determined the particle  
146 size distribution of each IRD-sized lithology in triplicate using a Mastersizer 3000. Samples were  
147 measured for 20 seconds at a stirring speed of 2500 rpm with ultrasound applied for 40 seconds  
148 prior to measurement.

149

150 The matrix of our phantoms derives from a pelagic multi core (GS15-198-62MC-F) retrieved off  
151 the Iceland Plateau (70°01'N 13°33'W) at 1423 m water depth (Jansen & Cruise-Members,  
152 2015). To avoid introducing noise to the experiment, all IRD-sized particles were removed a-  
153 priori by sieving the sediment through a 63 µm mesh. Further, treatment with 1M acetic acid at  
154 50 °C (until reaction ceased) dissolved in-situ calcite shells. To each sample box, we added  
155 approximately 6 grams of matrix mixed with 5 ml water to emulate the properties of natural  
156 marine sediments. In addition to the aforementioned known number of IRD-sized grains,

157 phantoms were spiked with ~600 foraminifera shells of arbitrary species larger than 150  $\mu\text{m}$   
158 from the Norwegian Sea (H. Halfidason, pers. comm.) to assess whether ubiquitous calcite shells  
159 introduce noise to CT IRD counts. The potential error margin related to loss of material during  
160 mixing and transfer of material was estimated at 0.31 g ( $2\sigma = 0.61\text{g}$ ), by weighing the box after  
161 finalizing it. Finally, we ascertained the Dry Bulk Density (DBD) of our phantoms following the  
162 approach of Dean Jr (1974) to convert CT-counted particles per volume data to particles per  
163 gram of dry weight conform most studies.

164

## 165 **2.2 Natural marine sediment cores**

166

167 To further test the potential of CT-based IRD-sized particle detection and counting, we applied  
168 the insights gained from our phantom experiment on two published conventionally analyzed IRD  
169 stratigraphies (2 cm counting resolution). These encompass two segments of North Atlantic  
170 calypso cores that were extracted on-board the R/V G.O. Sars ( Dokken & Cruise-Members,  
171 2016, Jansen & Cruise-Members, 2015): **1**) the 454-488.5 cm segment from core GS16-204-  
172 22CC-A ( $58^\circ 2.830'\text{N}$ ,  $47^\circ 2.360'\text{W}$ : 3160 m water depth), which was previously investigated by  
173 Griem et al. (2019), and **2**) the 231-281 cm section of GS16-204-18CC ( $60^\circ 1.840'\text{N}$ ,  $40^\circ$   
174  $33.450'\text{W}$ : 2220 m water depth) (Rutledal et al., 2020). As detailed in section 3.2, we manually  
175 re-counted the 267.5-280 cm interval of the latter archive continuously at 0.5 cm resolution. Both  
176 cores were primarily selected because they have been analyzed using standardized IRD counting  
177 methods, show distinct variability, focus on the 150-500  $\mu\text{m}$  size range, and the number of  
178 counted particles falls within the range of our experimental design ( $<2000$  IRD  $\text{g}^{-1}$  dry sediment).  
179 To optimize scanning resolution by minimizing the distance between source and detector (see  
180 van der Bilt et al. 2021), we extracted 2 cm wide u-channels from both sediment cores for CT

181 scanning. As with our phantoms (see section 2.2), we relied on DBD measurements after Dean Jr  
182 (1974) to convert CT-derived counts per volume to particles per gram dry weight. To this end,  
183 we extracted one sample near the top and bottom of the homogenous scanned section from  
184 GS16-204-22CC, while extracting four samples from the investigated segment of GS16-204-  
185 18CC due to a lithological change at 259 cm core depth as reported in Dokken & Cruise-  
186 Members (2016).

### 187 **2.3 CT scanning**

188

189 Fundamentally, Computed Tomography (CT) can resolve objects based on differences in X-Ray  
190 absorption: X-Ray photons penetrate light (black; radiolucent) materials with ease, while  
191 radiation is absorbed by dense (white; radiopaque) matter like bone (Röntgen, 1896), or clastic  
192 particles (Fig. 1B). The degree of X-Ray attenuation is captured by grayscale values, who  
193 typically reflect material density (higher is denser). By rotating objects or an X-Ray source and  
194 detector, CT scanners generate large numbers of 2-D radiographs known as orthoslices from  
195 various angles. These images can be reconstructed to create 3-D visualizations or reconstructions  
196 (e.g. Kalender, 2011). In contrast with more established 2-D X-Ray-based IRD detection  
197 approaches (e.g. Grobe, 1987), this allows characterization and counting of particles per volume.

198

199 For this study, CT scanning was performed using a ProCon CT-ALPHA-CORE system located  
200 at the Earth Surface Sediment Laboratory (EARTHLAB) of the University of Bergen that is  
201 customized for whole-core (max. 150 cm) analysis (see e.g. van der Bilt et al., 2018). This one-  
202 of-its-kind 16-bit scanner is fitted with a 240 kV microfocus X-Ray source and 9 MP detector  
203 that move vertically while the scanned object rotates. All presented scans were scanned at 800  
204  $\mu\text{A}$  and 100 kV with an exposure time of 334 ms to generate 1600 projections per rotation. This

205 relatively high current helps us minimize the imprint of photoelectric effect (Duliu, 1999). A  
206 physical 0.5 mm Cu filter was applied to reduce beam hardening effects (see Brooks & Di Chiro,  
207 1976), as well as ring artifact correction and median filtering. Using 2 cm wide u-channels and  
208 boxes allowed us to optimize scanning resolution by minimizing the distance between source and  
209 detector, producing imagery at  $\sim 21 \mu\text{m}$  isotropic voxel size.

210

## 211 **2.4 CT processing**

212

213 After scanning, CT projections were reconstructed for 3-D visualization with the Fraunhofer  
214 Volex X-Ray Office software. To further minimize the imprint of CT artifacts like beam  
215 hardening or edge effects (e.g. Barrett & Keat, 2004 and section 2.4), we cropped  $\sim 1 \text{ cm}^3$   
216 volumes near the center of scanned boxes and  $1 \text{ cm}^2$  wide sections of the u-channels. This step  
217 was performed in duplicate (henceforth referred to as samples A and B) to assess the  
218 representativeness of these 3-D cutouts. All subsequent image analyses were executed using  
219 version 9.1.1 of Thermo Scientific Avizo. To broaden the applicability of our approach, we  
220 relied on basic image processing techniques that are accessible to most geoscientists (see Fig.  
221 S3). All applied tools and modules are highlighted in *italics* below and briefly described to help  
222 users execute the same steps in other often-used image processing suites like ImageJ or  
223 VGStudio Max. We first applied an iterative routine using the *Colormap* editor to highlight  
224 clastic particles from background host sediments. This simple approach fundamentally relies on  
225 the subtle but measurable density differences between both materials and the shape of the clastic  
226 particles; as can be seen in Fig. 1C, the porous (water-soaked) matrix is significantly lighter  
227 (darker) than dense (white) clasts. We then isolated the designated CT density range using the  
228 *Interactive Threshold* segmentation tool. As can be seen in Fig. 1B, this binary image does not

229 adequately resolve the edge of clasts – a prerequisite when counting specific size fractions for  
230 IRD analysis. The observed noise is introduced by partial volume effects: the inter-voxel blurring  
231 of CT greyscale values along the steep density gradient between different materials (e.g. Glover  
232 & Pelc, 1980, Schlüter et al., 2010). To overcome this issue, we restored object boundaries with  
233 a combination of dilation and erosion using the *Closing* module as shown in Fig. 1D. Next, the  
234 *Separate Objects* module was applied to make sure that adjoining or coagulating particles are  
235 split as can be seen in Fig. 1E.

236 Following the above steps to detect and resolve particles, we individually characterized them for  
237 analysis with the *Label Analysis* module (Fig. 1F). During this step, the equivalent diameter and  
238 shape properties of each object was calculated using the *EqDiameter* and *Shape\_Va3D* measures,  
239 along with the coordinates (*BaryCentre*) of grains. We used the *Shape\_Va3D*-measurement to  
240 account for the fact that non-spherical objects may pass through a sieve mesh that is larger than  
241 their equivalent diameter if oriented towards their smallest projection (see e.g. Retsch, 2009). To  
242 do so, we normalized our 150  $\mu\text{m}$  size threshold (see sections 2.1-2) against the degree of non-  
243 sphericity reflected by *Shape\_Va3D* values  $>1$ . 'Digital sieving' was performed using the *Sieve*  
244 *Analysis* module before summing up particle counts for each phantom and at 1 mm depth  
245 intervals in scanned core sections. Finally, we performed basic geostatistical analyses like re-  
246 sampling, correlation and linear regression using version 16 of the StataSE software.

247

## 248 **3 Results and discussion**

249

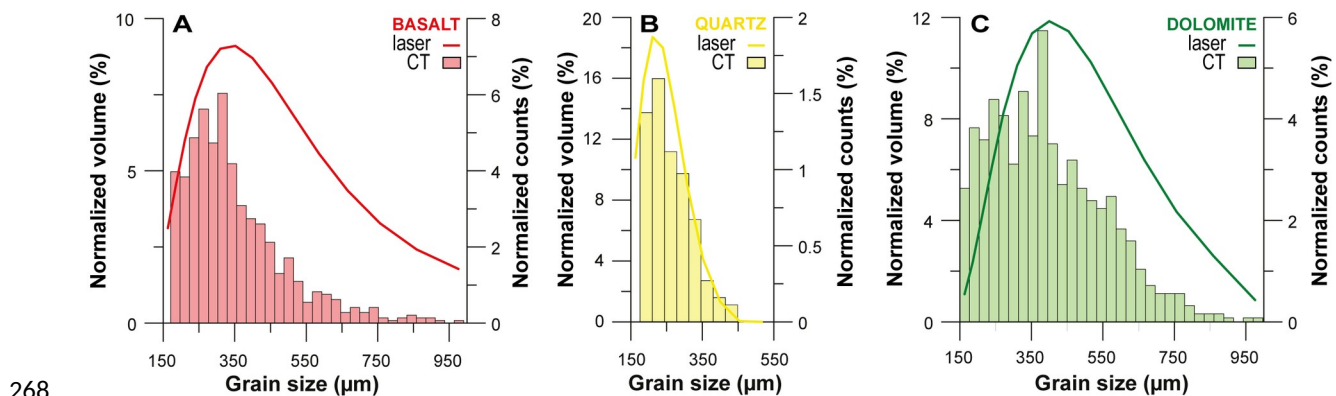
### 250 **3.1 Experimental findings**

251

252 **3.1.1 Particle size analysis**

253

254 The correct identification of a known number of particles within a specific size range is of  
 255 fundamental importance to this study. Therefore, we compared CT particle counts on all  
 256 phantoms spiked with  $\sim 1000$  grains ( $>150 \mu\text{m}$ ) per  $\text{g}^{-1}$  dry sediment to laser diffraction  
 257 measurements of pure extracts of each lithology used to spike these synthetic archives (section  
 258 2.1). Intercomparability is aided by the fact that both these approaches calculate the equivalent  
 259 diameter of a sphere with the same volume for each particle. CT counts were corrected with the  
 260 *Shape\_Va3D* measure to account for the possibility that non-spherical objects may pass through  
 261 a sieve mesh that is larger than their equivalent diameter (see section 2.4 and Fig. S3). As can be  
 262 seen in Fig. 2, there is close agreement between CT and laser-derived Particle Size Distributions  
 263 (PSDs). These findings **1)** strengthen our confidence that the CT processing steps applied in this  
 264 study accurately constrain the distribution of size fractions commonly targeted for IRD analysis  
 265 – a prerequisite for automatic counting, **2)** open doors for future venture into non-destructive CT-  
 266 based particle size analysis, and **3)** highlight differences between PSDs of the lithologies used to  
 267 spike our phantoms to help contextualize possible counting offsets in the following paragraphs.



269 **Figure 2.** Comparing laser diffraction (Mastersizer: line) and CT-derived (bars) particle size  
 270 distributions for IRD-sized grains of each bedrock type used to spike our phantoms: basalt (a),

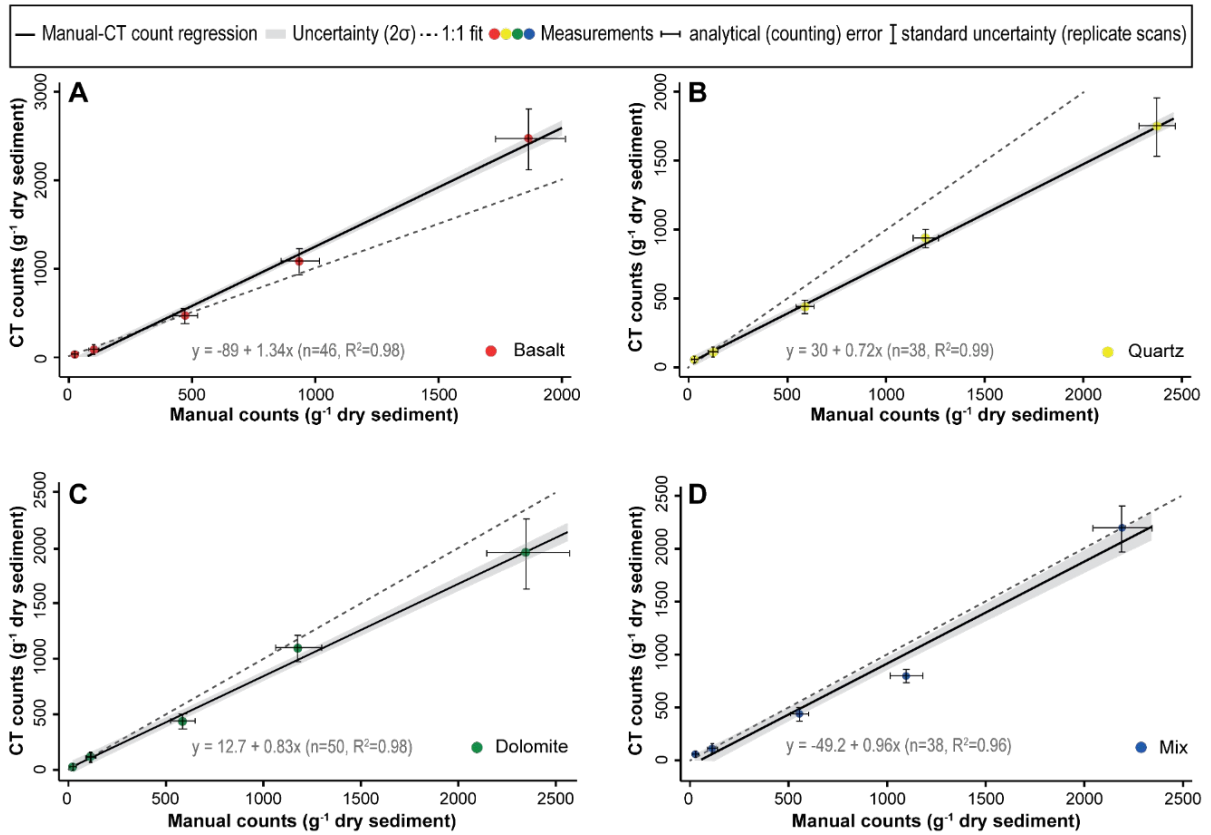
271 quartz (**b**) and dolomite (**c**). The former data are expressed as a normalized volume (%), while  
272 the latter are calculated as normalized counts (%). See section 2.1 for additional details.

273

### 274 **3.1.2 Lithic grain counting**

275

276 As shown in Fig. 3, all linear regression fits between manual and CT counts in our phantoms are  
277 highly significant ( $R^2 = 0.96-0.99$ ,  $p = 0.00$ ), regardless of the lithology of added grains. Besides  
278 demonstrating the potential of CT scanning to automatically count IRD-sized particles, these  
279 findings also allay concerns that calcite shells introduce noise: the high reproducibility of lower  
280 counts in particular show that the ~600 foraminifera shells added to each phantom were not CT-  
281 counted. We attribute this to partial volume effects: while the density of calcium carbonate (2.7  
282  $\text{g/cm}^3$ ) is near-identical to that of the rock types of added grains (2.65-3  $\text{g/cm}^3$ ), voxel blurring  
283 with air-, water or matrix-filled chambers of foraminiferal tests yield a lower density (section  
284 2.4).



285

286 **Figure 3.** Linear regression fits (and summary statistics) between manual and CT counts of IRD-  
 287 sized (150-500 μm) particles in synthetic sediment records (phantoms) spiked with basalt (a),  
 288 Quartz (b), Dolomite (c) and a 1:1:1 mixture of each (d). See section 2.1 for additional details.

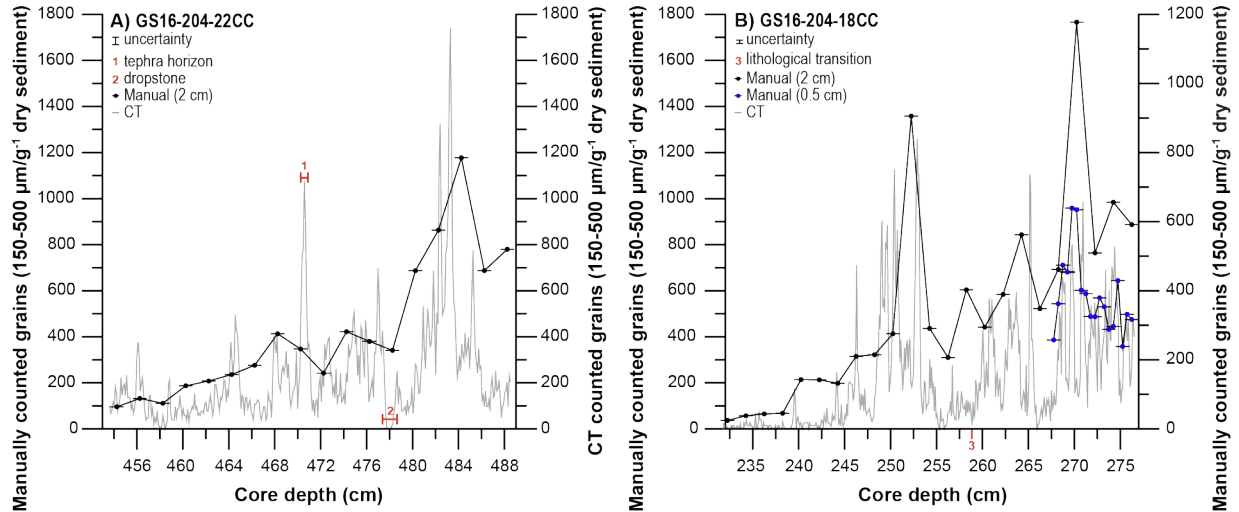
289

290 Our experimental findings compare favorably with previous efforts to (semi)-automatically count  
 291 particles. Fouinat et al. (2017), for example, applied a similar CT-based approach to count larger  
 292 mm-scale particles in a silty matrix, but derive a poorer fit ( $R^2 = 0.66$ ,  $p = 0.015$ ). We argue that  
 293 this weaker correspondence can be primarily attributed to a lower scanning resolution of 0.25  
 294 mm versus 21 μm in our study (section 2.3). Becker et al. (2018) employed an approach based  
 295 on automated microscopy to derive a marginally lower goodness-of-fit ( $R^2 = 0.94$ ). However,

296 this approach still requires destructive (lower resolution) sampling and time-consuming wet  
297 sieving.

298

299 However, while our experimental findings are promising, systematic offsets exist between  
300 manual and CT counts. While highly significant, the slopes of all fits deviate from a 1:1 relation:  
301 as seen in Fig. 3, these offsets often exceed calculated counting errors (sections 2.1 and 2.4) for  
302 all lithologies, but especially for quartz. Here, we tentatively attribute these errors to a number of  
303 analytical sources. Firstly, differences in the PSD of lithic grains. Assuming a unimodal  
304 distribution (to estimate the proportion of sieved-out particles  $<150\ \mu\text{m}$  – see section 2.1), a  
305 significant percentage of grains may be included or excluded when object boundaries (and thus  
306 diameters) are incorrectly resolved during CT processing (see section 2.4 and Figs. 1C-E). This  
307 source of error may well explain why offsets are largest for quartz as **1**) the median PSD of this  
308 lithology sits closest to our  $150\ \mu\text{m}$  cut-off (Fig. 3B) so that small errors generate large count  
309 uncertainties, and **2**) density differences with host sediments are smallest, which complicates our  
310 efforts to accurately resolve object boundaries based on CT greyscale values (see section 2.4). In  
311 addition, image processing may also impact CT particle counts by erroneously splitting  
312 irregularly shaped grains into multiple objects with the *Separation* module (see Fig. 1E). This  
313 source of error may help explain the observed overestimation of basaltic grains by CT counting  
314 (Fig. 3A). This notion is supported by **1**) visual evidence of the irregular shape of these particles  
315 (see Fig. S1), and **2**) their comparatively large size (Fig. 2A), which increases the probability that  
316 erroneously split particles are included in the counted  $>150\ \mu\text{m}$  fraction. The applied *Closing*  
317 *module* (see section 2.4) might also have exacerbated this effect as it may expand the size of  
318 particles by smoothing uneven surfaces or filling in hollow particles (see Figs. 1C-D).



319

320 **Figure 4.** A comparison of manual and CT-derived counts of IRD-sized particles in two marine

321 sediment segments. For (a) GS16-204-22CC and (b) GS16-204-18CC. Highlighted uncertainty

322 intervals (grey) are based on the average offset in CT-derived grain counts between replicate 3-D

323 samples A and B (see section 2.4). Horizontal bars on manual count symbols mark the 0.5 cm

324 sampling width (see section 2.2). Red numerals indicate the stratigraphic position of marked

325 features in the scanned core segments – 1) the NAAZ II tephra marker (Rutledal et al., 2020), 2)

326 a cm-scale drop stone, and 3) a visible lithological transition (Dokken &amp; Cruise-Members, 2016).

327

328 **3.2 Application on manually counted natural sediment archives.**

329

330 As can be seen in Fig. 4, our CT-based approach to count 150-500 µm particles capture most of

331 the main IRD peaks in the manually counted records. The strength of this relation is confirmed

332 by positive Spearman  $\rho$  values of 0.75 ( $n=18$ ,  $p=0.0003$ ) for core GS16-204-22CC and 0.63333 ( $n=25$ ,  $p=0.0007$ ) for core GS16-204-18CC – all calculated on evenly (0.5 cm) resampled data.

334 These findings clearly demonstrate the potential of our CT-based approach to semi-automatically

335 detect the 150-500  $\mu\text{m}$ -sized particles that are typically targeted in IRD studies, even at  
336 comparatively low concentrations (max. 1800 grains/gr).

337

338 However, while certainly encouraging, the presented results also reveal substantial disparities.  
339 These can partly be explained by differences in sampling resolution: grains were CT-counted at  
340 0.1 cm intervals, while 0.5 cm wide samples were taken every 2 cm for manual counts –  
341 smoothing out high-frequency (mm-scale) variability. As can be seen in Fig. 4B, an improved  
342 0.5 cm sampling resolution greatly improves the agreement between manual and CT counts.  
343 Indeed, correlation of both datasets using the most similar CT-derived grain numbers within the  
344 0.5 cm sampling width of manual samples yields a Spearman  $\rho$  of 0.96 ( $n=18$ ,  $p=0.0000$ ) – a  
345 result that equals the robustness of our experimental findings (see section 3.1.2). In addition, our  
346 scanned u-channel from GS16-204-22C contains two features that are also highlighted using the  
347 applied segmentation approach (see section 2.4) due to their highly similar density: the basaltic-  
348 component of a NAAZ II tephra deposit and a large drop stone (see Fig. 4A: 1 and 2). The latter  
349 is not CT-counted as its size falls outside our specified 150-500  $\mu\text{m}$  grain range (see section 2.1),  
350 but its size simply leaves less space for other particles within the 0.1  $\text{cm}^3$  sample slice - creating  
351 a distinct minimum in counted particles. The tephra is captured by a sharp peak in the CT-  
352 counted IRD record. To remedy this, the characteristically high concentration of particles (ash  
353 shards) in tephra deposits may be highlighted using down-core variations in CT grayscale values  
354 as outlined by van der Bilt et al. (2021). The structural offset between CT and manual counts,  
355 which particularly affects GS16-204-18CC as seen in Fig. 4B, is more difficult to account for. As  
356 both cores were counted by the same analyst and derive from the same area (see section 2.1), we  
357 preclude differences in human counting error and lithology-specific analytical errors (see section

358 3.1.2) as plausible explanations. Because the bedrock geology of proximal IRD source areas in  
359 the region is dominated by quartz-rich metamorphic bedrock types (Dawes, 2009), it is worth  
360 noting that the offset between evenly sampled CT and manual counts in GS16-204-22CC is  
361 identical (28%) to the difference found in our quartz-spiked phantoms. But why this mismatch  
362 far greater in GS16-204-18CC, where our CT-based approach captures just 40% of manually  
363 counted grains (Fig. 4B)? We argue that the dissimilarity between both datasets may be  
364 attributed to disturbance introduced by bioturbation. In recent years, numerous researchers have  
365 harnessed various imaging techniques to demonstrate that burrowing may extensively modify the  
366 sediment structure and blur IRD signals (e.g., Dorador et al., 2014, Hodell et al., 2017). Indeed,  
367 Rutledal et al. (2020) relied on the same threshold-based segmentation routine presented in  
368 section 2.4 to highlight the presence of air-filled burrows in GS16-204-18CC and GS16-204-  
369 22CC. As can be seen in Fig. S4, these features are particularly extensive in the section of GS16-  
370 204-18CC scanned for this study. Furthermore, closer inspection of the appended X-Ray images  
371 shown in Fig. S4 reveals additional deformational structures that may represent infilled trace  
372 fossils or burrows. As these features are distributed both horizontally and vertically, the lateral  
373 offset between manually counted samples and scanned u-channels could have a major impact on  
374 down-core IRD profiles. To test this, we compared our CT data from GS16-204-18CC to higher-  
375 resolution manual counts performed on the same u-channel. As can be seen in Fig. 4B, the offset  
376 between these data is significantly smaller and is similar (39%) to the difference found between  
377 counts and scans in our quartz-spiked phantoms (28%).

378

#### 379 **4 Conclusions**

380

381 This work underscores the potential of CT scanning for semi-automated and non-destructive  
382 counting of IRD-sized (150-500  $\mu\text{m}$ ) grains in sediment archives. Notwithstanding analytical  
383 errors that we ascribe to image processing artefacts, our experimental findings show that CT  
384 numbers capture more than 95% of grain count variability in homogenous phantoms. Also, by  
385 spiking each of these synthetic samples with a known number of foraminiferal tests, we allay  
386 concerns that (often-ubiquitous) calcite shells of a similar size and density affect CT IRD counts.  
387 Despite evidence of bioturbation and differences in sampling resolution, CT-derived counts  
388 strongly correlate ( $\rho = 0.63\text{-}0.75$ ) with manual IRD profiles in both scanned core sections.  
389 Moreover, quadrupling our manual counting resolution on CT-scanned u-channels minimizes  
390 offsets between both datasets ( $\rho = 0.96$ ). This somewhat surprising result suggests that mm-scale  
391 CT variations capture a signal rather than noise and highlights how bioturbation may modify  
392 IRD profiles. Importantly, all our results were acquired using basic image processing techniques  
393 that can be quickly mastered by most geologists. Following from the above, we argue that the  
394 presented CT-based counting approach significantly benefit IRD investigations by preserving  
395 material, improving sampling resolution, and optimizing lab workflows. By enabling faster  
396 detection of higher-frequency IRD events, these advances have significant potential to deepen  
397 our understanding of climate-ice sheet interactions on human-relevant timescales.

398

### 399 **Acknowledgments**

400

401 We want to express our gratitude to the Trond Mohn Foundation and the Centre for Climate  
402 Dynamics for funding this research through their Starting Grant and Fast-Track initiative  
403 programs, respectively. We also acknowledge support from the European Research Council

404 under the European Community's Seventh Framework Program (FP7/2007-2013)/ERC grant  
 405 agreement 610055 as part of the Ice2ice project. Finally, we want to thank Lisa Griem for  
 406 providing manual counted IRD profiles for the scanned core segments, and Rick Hennekam as  
 407 well as Eystein Jansen for helping us improve this manuscript with his comments. *Data*  
 408 *availability statement*: we have archived all numerical data presented in the main manuscript in  
 409 the Dataverse repository, and these will be made available upon publication. For now, we have  
 410 attached a copy of this file as Supporting information for review purposes.

411

412 **References**

413

- 414 Andrews, J. T. (2000) Icebergs and iceberg rafted detritus (IRD) in the North Atlantic: facts and  
 415 assumptions. *Oceanography*, p. 100-108.
- 416 Andrews, J. T., Smith, L. M., Preston, R., Cooper, T. & Jennings, A. E. (1997) Spatial and  
 417 temporal patterns of iceberg rafting (IRD) along the East Greenland margin, ca. 68 N,  
 418 over the last 14 cal. ka. *Journal of Quaternary Science: Published for the Quaternary*  
 419 *Research Association*, 12 (1), p. 1-13. doi: 10.1002/(SICI)1099-  
 420 1417(199701/02)12:1<1::AID-JQS288>3.0.CO;2-T
- 421 Barrett, J. F. & Keat, N. (2004) Artifacts in CT: recognition and avoidance. *Radiographics*, 24  
 422 (6), p. 1679-1691. doi: 10.1148/rg.246045065
- 423 Becker, L. W. M., Hjelstuen, B. O., Støren, E. W. N. & Sejrup, H. P. (2018) Automated counting  
 424 of sand-sized particles in marine records. *Sedimentology*, 65 (3), p. 842-850. doi:  
 425 10.1111/sed.12407
- 426 Bond, G., Heinrich, H., Broecker, W., Labeyrie, L., McManus, J., Andrews, J., . . . Simet, C.  
 427 (1992) Evidence for massive discharges of icebergs into the North Atlantic ocean during  
 428 the last glacial period. *Nature*, 360 (6401), p. 245-249. doi: 10.1038/360245a0
- 429 Brooks, R. A. & Di Chiro, G. (1976) Beam hardening in x-ray reconstructive tomography.  
 430 *Physics in medicine & biology*, 21 (3), p. 390. doi: 10.1088/0031-9155/21/3/004
- 431 Dansgaard, W., Johnsen, S. J., Clausen, H. B., Dahl-Jensen, D., Gundestrup, N. S., Hammer, C.  
 432 U., . . . Jouzel, J. (1993) Evidence for general instability of past climate from a 250-kyr  
 433 ice-core record. *Nature*, 364 (6434), p. 218-220. doi: 10.1038/364218a0
- 434 Dawes, P. R. (2009) The bedrock geology under the Inland Ice: the next major challenge for  
 435 Greenland mapping. *Geological Survey of Denmark and Greenland (GEUS) Bulletin*, 17,  
 436 p. 57-60. doi: 10.34194/geusb.v17.5014
- 437 Dean Jr., W. E. (1974) Determination of carbonate and organic matter in calcareous sediments  
 438 and sedimentary rocks by loss on ignition: comparison with other methods. *Journal of*  
 439 *Sedimentary Research*, 44 (1). doi: 10.1306/74D729D2-2B21-11D7-8648000102C1865D

- 440 Dokken, T. M. & Cruise-Members (2016) Cruise report of cruise GS16-204 (Reykjavik-  
441 Narsarsuaq). In Dokken, T.M. (ed.): Bjercknes Climate Data Centre.
- 442 Dorador, J., Rodríguez-Tovar, F. J. & Expedition, IODP (2014) Quantitative estimation of  
443 bioturbation based on digital image analysis. *Marine Geology*, 349, p. 55-60. doi:  
444 10.1016/j.margeo.2014.01.003
- 445 Duluu, O. G. (1999) Computer axial tomography in geosciences: an overview. *Earth-science*  
446 *reviews*, 48 (4), p. 265-281. doi: 10.1016/S0012-8252(99)00056-2
- 447 Ekblom Johansson, F., Wangner, D. J., Andresen, C. S., Bakke, J., Støren, E. W. N., Schmidt, S.  
448 & Vieli, A. (2020) Glacier and ocean variability in Ata Sund, west Greenland, since 1400  
449 CE. *The Holocene*, 30 (12), p. 1681-1693. doi: 10.1177/0959683620950431
- 450 Fouinat, L., Sabatier, P., Poulenard, J., Reyss, J., Montet, X. & Arnaud, F. (2017) A new CT  
451 scan methodology to characterize a small aggregation gravel clast contained in a soft  
452 sediment matrix. *Earth Surface Dynamics*, 5 (1), p. 199-209. doi: 10.5194/esurf-5-199-  
453 2017
- 454 Glover, G. H. & Pelc, N. J. (1980) Nonlinear partial volume artifacts in x-ray computed  
455 tomography. *Medical physics*, 7 (3), p. 238-248. doi: 10.1118/1.594678
- 456 Griem, L., Voelker, A. H. L., Berben, S. M. P., Dokken, T. M. & Jansen, E. (2019) Insolation  
457 and Glacial Meltwater Influence on Sea–Ice and Circulation Variability in the  
458 Northeastern Labrador Sea During the Last Glacial Period. *Paleoceanography and*  
459 *Paleoclimatology*, 34 (11), p. 1689-1709. doi: 10.1029/2019PA003605
- 460 Grobe, H. (1987) A simple method for the determination of ice-rafted debris in sediment cores.  
461 *Polarforschung*, 57 (3), p. 123-126.
- 462 Heinrich, H. (1988) Origin and consequences of cyclic ice rafting in the northeast Atlantic Ocean  
463 during the past 130,000 years. *Quaternary research*, 29 (2), p. 142-152. doi:  
464 10.1016/0033-5894(88)90057-9
- 465 Hemming, S. R. (2004) Heinrich events: Massive late Pleistocene detritus layers of the North  
466 Atlantic and their global climate imprint. *Reviews of Geophysics*, 42 (1). doi:  
467 10.1029/2003RG000128
- 468 Hodell, D. A., Nicholl, J. A., Bontognali, T. R. R., Danino, S., Dorador, J., Dowdeswell, J.  
469 A., . . . Mleneck–Vautravers, M. J. (2017) Anatomy of Heinrich Layer 1 and its role in  
470 the last deglaciation. *Paleoceanography*, 32 (3), p. 284-303. doi: 10.1002/2016PA003028
- 471 Jansen, E. & Cruise-Members (2015) Cruise report of cruise GS15-198 (Reykjavik-Tromsø, July  
472 19–August 15 2015).
- 473 Jennings, A. E., Andrews, J. T., Cofaigh, C. Ó., St-Onge, G., Belt, S., Cabedo-Sanz, P., . . .  
474 Campbell, D. C. (2018) Baffin Bay paleoenvironments in the LGM and HS1: Resolving  
475 the ice-shelf question. *Marine Geology*, 402, p. 5-16. doi: 10.1016/j.margeo.2017.09.002
- 476 Jullien, E., Grousset, F. E., Hemming, S. R., Peck, V. L., Hall, I. R., Jeantet, C. & Billy, I. (2006)  
477 Contrasting conditions preceding MIS3 and MIS2 Heinrich events. *Global and Planetary*  
478 *Change*, 54 (3-4), p. 225-238. doi: 10.1016/j.gloplacha.2006.06.021
- 479 Kalender, W. A. (2011) *Computed tomography: fundamentals, system technology, image quality,*  
480 *applications*, Germany: Publicis Corporate Publishing.
- 481 Retsch, G. H. (2009) Sieve analysis taking a close look at quality.
- 482 Ruddiman, W. F. (1977) Late Quaternary deposition of ice-rafted sand in the subpolar North  
483 Atlantic (lat 40 to 65 N). *Geological Society of America Bulletin*, 88 (12), p. 1813-1827.  
484 doi: 10.1130/0016-7606(1977)88<1813:LQDOIS>2.0.CO;2

- 485 Rutledal, S., Berben, S. M. P., Dokken, T. M., Van Der Bilt, W. G. M., Cederstrøm, J. M. &  
486 Jansen, E. (2020) Tephra horizons identified in the western North Atlantic and Nordic  
487 Seas during the Last Glacial Period: Extending the marine tephra framework. *Quaternary*  
488 *Science Reviews*, p. 106247. doi:10.1016/j.quascirev.2020.106247
- 489 Röntgen, W. C. (1896) On a new kind of rays. *Science*, 3 (59), p. 227-231.
- 490 Røthe, T. O., Bakke, J., Støren, E. W. N. & Bradley, R. S. (2018) Reconstructing Holocene  
491 glacier and climate fluctuations from lake sediments in Vårfluesjøen, northern  
492 Spitsbergen. *Frontiers in Earth Science*, 6. doi: 10.3389/feart.2018.00091
- 493 Schlüter, S., Weller, U. & Vogel, H. (2010) Segmentation of X-ray microtomography images of  
494 soil using gradient masks. *Computers & Geosciences*, 36 (10), p. 1246-1251. doi:  
495 10.1016/j.cageo.2010.02.007
- 496 van der Bilt, W. G. M., Cederstrøm, J. M., Støren, E. W. N., Berben, S. M. P. & Rutledal, S.  
497 (2021) Rapid Tephra Identification in Geological Archives With Computed Tomography:  
498 Experimental Results and Natural Applications. *Front. Earth Sci*, 8, p. 622386. doi:  
499 10.3389/feart.2020.622386
- 500 van der Bilt, Willem G. M., Rea, B., Spagnolo, M., Roerdink, D., Jørgensen, S. & Bakke, J.  
501 (2018) Novel sedimentological fingerprints link shifting depositional processes to  
502 Holocene climate transitions in East Greenland. *Global and Planetary Change*. doi:  
503 10.1016/j.gloplacha.2018.03.007
- 504 Van der Plas, L. & Tobi, A. C. (1965) A chart for judging the reliability of point counting results.  
505 *American Journal of Science*, 263 (1), p. 87-90. doi: 10.2475/ajs.263.1.87  
506